scientific reports

Check for updates

OPEN

Ternary metal oxide nanocomposite for room temperature H_2S and SO_2 gas removal in wet conditions

Nishesh Kumar Gupta[1,2], Eun Ji Kim[1,2], Soyoung Baek[2], Jiyeol Bae[1,2]✉ & Kwang Soo Kim[1,2]✉

A ternary Mn–Zn–Fe oxide nanocomposite was fabricated by a one-step coprecipitation method for the remotion of H_2S and SO_2 gases at room temperature. The nanocomposite has ZnO, MnO_2, and ferrites with a surface area of 21.03 m^2 g^{-1}. The adsorbent was effective in mineralizing acidic sulfurous gases better in wet conditions. The material exhibited a maximum H_2S and SO_2 removal capacity of 1.31 and 0.49 mmol g^{-1}, respectively, in the optimized experimental conditions. The spectroscopic analyses confirmed the formation of sulfide, sulfur, and sulfite as the mineralized products of H_2S. Additionally, the nanocomposite could convert SO_2 to sulfate as the sole oxidation by-product. The oxidation of these toxic gases was driven by the dissolution and dissociation of gas molecules in surface adsorbed water, followed by the redox behaviour of transition metal ions in the presence of molecular oxygen and water. Thus, the study presented a potential nanocomposite adsorbent for deep desulfurization applications.

Air contamination is a global issue which has been amplified by various anthropogenic activities in the last many decades. Among numerous air contaminants toxifying the air, hydrogen sulfide (H_2S) and sulfur dioxide (SO_2) has known to cause severe damage to human health and the environment. H_2S is a toxic pungent-smelling gas released from decayed organic matter, oil industry, coal and natural gas-based thermal power plants, and sewage treatment facilities[1,2]. Acute exposure to H_2S at levels of 200–500 ppm could paralyze the olfactory nerve and beyond 500 ppm could lead to sudden death[2,3]. Furthermore, H_2S conversion to SO_2 and its hydrolysis to form acid rain could acidify soil and water bodies, which could be disastrous to plants and marine life, respectively[4,5]. SO_2 is a colourless toxic gas with a sharp odour, which could cause various respiratory ailments such as chronic bronchitis and infections of the respiratory tract[6]. While a low SO_2 concentration of 1–5 ppm is enough for human discomfort, exposure above 100 ppm could be life-threatening[7]. The main sources of atmospheric SO_2 are thermal power plants and vehicular emissions[8]. Thus, H_2S and SO_2 removal from point of origin should be prioritized to limit air contamination and prevent catastrophic events like smog formation and acid rain.

Chemical adsorption of these toxic gases over an adsorbent surface is one of the most simplistic and affordable methods to adsorb and mineralize H_2S and SO_2 gases to non-toxic by-products like sulfur and sulfates[9]. Moreover, chemisorption is highly efficient for flue gas desulfurization and natural gas purification applications, which are challenging, fundamentally and monetary-wise[1,10]. For this purpose, metal oxides have shown great potential due to the presence of weak basic sites (lattice oxygen) and basic OH^- groups, which could react with acidic gases like H_2S and SO_2 (acting as electron donors)[11,12]. The surface reactivity of metal oxides for these gases could be amplified in the presence of water molecules. Firstly, the water layer on the metal oxide surface dissociatively reacts and improves the hydroxyl density. Secondly, the surface water film dissolves the gas molecules, which lowers the energy barrier for reactive interaction with the metal oxide surface and thus favours the overall chemisorption process[13–17]. Thus, it is worth exploring the positive effect of water during the adsorption of acidic gases over metal oxides, which is the focus of this research work. Also, it is equally important to explore adsorbent materials for the remediation of low H_2S/SO_2 concentrates to confirm the applicability of adsorbents in deep desulfurization and gas purification applications.

In this study, we have fabricated an affordable Mn-Zn-Fe metal oxide nanocomposite by a one-step coprecipitation method for room-temperature adsorptive removal of H_2S and SO_2 gases in wet conditions. The gas

[1]Department of Environmental Research, University of Science and Technology (UST), Daejeon 34113, Korea. [2]Department of Environmental Research, Korea Institute of Civil Engineering and Building Technology (KICT), Goyang 10223, Korea. ✉email: baejiyeol@kict.re.kr; kskim@kict.re.kr

concentration of 500 and 100 ppm for H_2S and SO_2 was adopted for their industrial application and suitability in capturing these pollutants in the toxicity range for humans. The oxide showed better adsorption performance in wet conditions with complete mineralization to non-toxic by-products. Besides studying the factors affecting the adsorption process, the adsorption mechanism was studied in detail using various microscopic and spectroscopic techniques. The study confirmed that the oxide nanocomposite has the potential to eliminate and mineralize low concentrations of gaseous H_2S and SO_2 in dry–wet conditions.

Methods

Chemicals. Manganese(II) nitrate tetrahydrate ($Mn(NO_3)_2{\cdot}4H_2O$), zinc(II) nitrate hexahydrate ($Zn(NO_3)_2{\cdot}6H_2O$), iron(III) nitrate nonahydrate ($Fe(NO_3)_3{\cdot}9H_2O$), and 2.0 mol L^{-1} NaOH solution were procured from Samchum Pure Chemicals, Korea. H_2S gas (0.05 Vol.%) and SO_2 gas (0.01 Vol.%) balanced with pure N_2 gas were procured from Union gas, Korea. All solutions were prepared in double-distilled water.

Synthesis of nanocomposite. In 50 mL of deionized water, 3.76 g of $Mn(NO_3)_2{\cdot}4H_2O$, 4.45 g of $Zn(NO_3)_2{\cdot}6H_2O$, and 4.04 g of $Fe(NO_3)_3{\cdot}9H_2O$ were dissolved to give a final Mn^{2+}:Zn^{2+}:Fe^{3+} ratio of 3:3:2. A higher ratio of divalent to trivalent cations was adopted for the formation of MnO_2 and ZnO in the nanocomposite (for a higher acidic gas adsorption capacity). Under vigorous stirring, 2.0 mol L^{-1} NaOH solution was added dropwise until the solution pH reached 12.5. This pH was sufficient for the formation of ternary oxide nanocomposites as reported earlier[18]. After stirring for 2 h, the precipitate was phase separated and dried at 393 K overnight in a hot air oven. The use of an excess of water for washing was avoided to reduce the overall impact on the environment during the material fabrication process.

Analytical instruments. The morphology in the surface and transmission mode was probed over field emission scanning electron microscopy (FE-SEM, Hitachi S-4300, Hitachi, Japan) and field emission TEM (FE-TEM, JEM-2010F, JEOL Ltd., Japan), respectively. SEM analysis was done on finely grounded dried samples after coating them with a gold-platinum alloy by ion-sputtering (E-1048 Hitachi ion sputter). The elemental analysis was done using energy-dispersive X-ray spectroscopy (EDAX, X-Maxn 80 T, Oxford Instruments, United Kingdom). The specific surface area and porosity were determined by analysing the standard N_2 adsorption–desorption isotherm at 77 K using a Gemini 2360 series (Micromeritics, Norcross, United States) instrument after degassing at 423 K for 6 h with a mass of 0.324 g. The powder X-ray diffraction (PXRD) patterns were obtained at room temperature ($2\theta = 5–50°$) on an Ultima IV (Rigaku, Japan) X-ray diffractometer with Cu Kα radiation ($\lambda = 1.5406$ Å) and a Ni filter. Fourier-transform infrared (FTIR) spectra of samples were recorded using KBr pellets over a Cary670 FTIR spectrometer (Agilent Technologies, United States). For X-ray photoelectron spectroscopy (XPS) analysis, a K-alpha XPS instrument (Thermo Fisher Scientific, United Kingdom) was used with a monochromatic Al K_α X-ray source. The pressure was fixed to 4.8×10^{-9} mbar. Spectra were charge corrected to the main line of the C 1 s (aromatic carbon) set to 284.7 eV. Spectra were analysed using CasaXPS software (version 2.3.14).

Breakthrough protocol. The gas adsorption experiments were performed by taking 0.5 g of the adsorbent in a Pyrex tube (height: 50 cm and diameter: 1 cm) at 298 K. The sample was fixed between the glass wool and supported on silica beads[19]. The H_2S gas (0.05 Vol.%) or SO_2 gas (0.01 Vol.%) was passed through it at a fixed flow rate. The outgoing gas was analyzed using an H_2S gas analyzer (GSR-310, Sensoronic, Korea) or an SO_2 gas analyzer (GASTIGER 6000, Wandi, Korea). The analyzer recorded the effluent gas concentration every minute in real-time until the breakthrough points of 20% (100 ppm for H_2S and 20 ppm for SO_2) were reached and after that the experiment was completed. The wet samples were prepared by passing water vapours (80% relative humidity) directly through the adsorbent bed before passing the gas through it. The gas adsorption capacity was measured using the following equation:

$$q = \frac{C_0 Q}{m} \int_0^{t_b} \left(1 - \frac{C_t}{C_0}\right) dt \tag{1}$$

where C_0-initial concentration (mg L^{-1}), C-concentration at time 't' (mg L^{-1}), Q-flowrate (L min^{-1}), m-the mass of adsorbent (g), and t_b-breakthrough time (s).

Results and discussion

The SEM micrograph of oxide nanocomposite showed irregularly shaped nano-globules, which were uniformly distributed in the entire region (Fig. 1a). The controlled release of base (precipitation agent) assisted in regulating the nucleation and particle growth kinetics, which prevented the aggregation of metal oxides in the ternary nanocomposite. A more detailed investigation of morphology was conducted over high-resolution TEM, which confirmed that the nano-globules were constructed of polyhedral nanoparticles (Fig. 1b). The crystallite planes of nanoparticles were assigned by measuring the fringe width and correlating with the interplanar spacing (d) values from the XRD pattern. The fringe width of 0.308, 0.530, and 0.261 nm were assigned to the MnO_2 (110)[20], ZnO (0002)[21], and MFe_2O_4 (311)[22], respectively. The EDAX elemental analysis confirmed peaks for Mn, Zn, Fe, and O at respective energies having the atomic contribution of 13.80, 7.14, 3.57, and 75.48%, respectively (Fig. 1c). The 2D elemental mapping showed an abundant density of Mn and Zn with low-density regions in the 'Fe' map (respective high-density regions marked in 'Mn' and 'Zn' maps). The possible reason for such a distribution could be the formation of pure, binary, and ternary metal oxides in the nanocomposite (Fig. 1d).

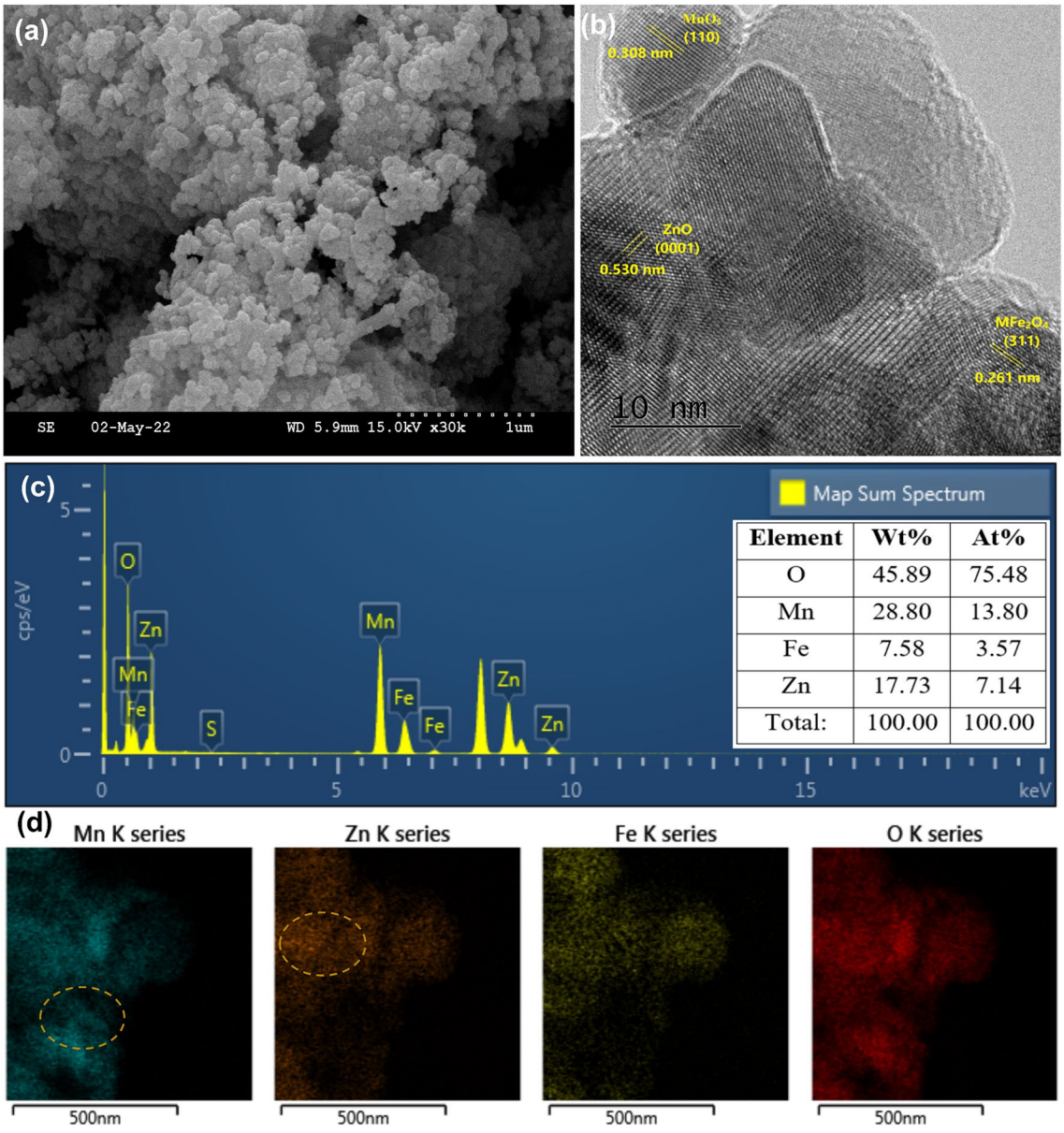

Figure 1. (**a**) SEM micrograph; (**b**) high-resolution TEM micrograph; (**c**) elemental distribution analysis; (**d**) 2D elemental mapping of MZFO.

The PXRD pattern of MFZO nanocomposite has diffraction peaks for β-MnO_2 (purple circle)[23], ZnO (pink circle)[24], ferrites (green square)[25], and $NaNO_3$ (blue square)[26], which confirmed a poly-oxide nature of the composite (Fig. 2a). A similar report is available for the fabrication of Cu–Zn-Mn ternary oxide nanocomposite, where CuO, ZnO, and MnO_2 nanoparticles were confirmed[18]. The absence of a washing step during the MFZO fabrication was responsible for the presence of $NaNO_3$ in the sample. The N_2 adsorption–desorption isotherm of MFZO nanocomposite exhibited a Type III behaviour, generally expected in macro-porous materials (Fig. 2b)[23]. The nanocomposite possessed a BET surface area of 21.03 $m^2\ g^{-1}$ and a pore volume of 0.07 $cm^3\ g^{-1}$. These values are higher than other nanocomposites like Mn_2O_3/Fe_2O_3 (6.18 $m^2\ g^{-1}$, 0.12 $cm^3\ g^{-1}$)[27], $CeO_2/Mn_2O_3/Fe_2O_3$ (15.64 $m^2\ g^{-1}$, 0.09 $cm^3\ g^{-1}$)[28], and Fe_2O_3/Na_2SO_4 (2.89 $m^2\ g^{-1}$, 0.01 $cm^3\ g^{-1}$)[29] used for the same applications. The spectrum has a broad band centred at 621 cm^{-1} for the metal–oxygen stretching vibrations[30,31]. The bands at 835 and 1385 cm^{-1} were attributed to the asymmetric stretching vibration (ν_3-NO_3^-) and out-of-plane bending vibration (ν_2-NO_3^-), respectively, of nitrate[32]. The bands at 3433 and 1635 cm^{-1} were assigned to the stretching and bending vibration modes of adsorbed water molecules, respectively (Fig. 2c)[33]. The XPS survey of MFZO confirmed peaks for Na 1 s, Zn 2p, Fe 2p, Mn 2p, O 1 s, and N 1 s at their respective binding energy. The Na 1 s and N 1 s peaks were associated with the presence of $NaNO_3$ (Fig. 2d).

The HRXPS Mn $2p_{3/2}$ signal of MFZO deconvoluted into three contributions at 640.7, 641.6, and 642.8 eV for Mn^{2+} (23.2%), Mn^{3+} (43.9%), and Mn^{4+} (32.9%) oxidation states of Mn ions, respectively[34]. The analyses showed that multivalent Mn ions were related to the formation of MnO_2 and Mn-based ferrites (Fig. 3a, Table S1). The HRXPS Zn 2p spectrum has two peaks at 1021.4 and 1044.3 eV for $2p_{3/2}$ and $2p_{1/2}$ signals of Zn^{2+} ions,

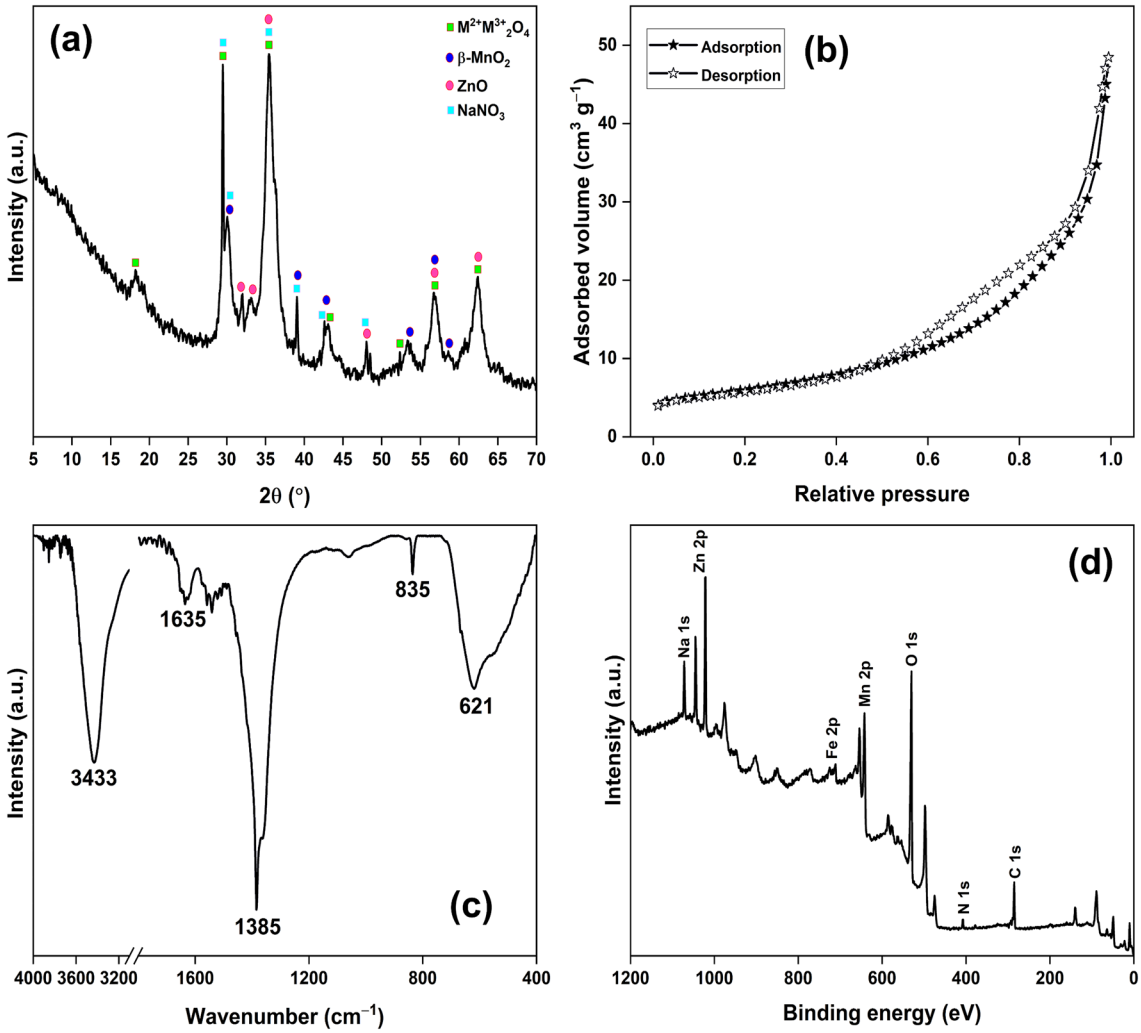

Figure 2. (**a**) PXRD pattern; (**b**) N_2 adsorption–desorption isotherm; (**c**) FTIR spectrum; (**d**) XPS survey of MZFO.

respectively (Fig. 3b, Table S2)[35]. In the HRXPS Fe 2p spectrum, the $2p_{3/2}$ signal was deconvoluted into two contributions at 710.8 and 712.9 eV for Fe^{2+} (70.4%) and Fe^{3+} ions (29.6%), respectively (Fig. 3c, Table S3)[36]. These two contributions were due to the formation of ferrites. The HRXPS O 1 s spectrum has three deconvoluted peaks at 530.0, 531.4, and 532.9 eV for lattice oxygen (56.9%), surface hydroxyl groups/nitrate ions (24.6%), and water molecules (18.4%), respectively (Fig. 3d, Table S4)[37].

The synthesized nanocomposite was tested for H_2S removal in breakthrough columns both in dry and wet conditions (Fig. 4a). The adsorption capacity of 0.73 mmol g^{-1} was achieved in the dry condition. However, in the wet condition, the capacity increased to 1.03 mmol g^{-1}, showing the positive role of water in the adsorption process mediated by the dissolution and dissociation of H_2S molecules in the water film over the oxide surface. The effect of parameters, *i.e.*, gas flow rate (Fig. 4b) and adsorbent loading (Fig. 4c) on the adsorption capacity was studied in the wet conditions. The adsorption capacity decreased with the increasing flow rate, where the highest capacity of 1.21 mmol g^{-1} was achieved with a flow rate of 0.1 L min^{-1}. Increasing flow rate disfavoured the adsorbate-adsorbent interaction due to a lowering in the gas retention time, which negatively impacted the capacity[38]. The adsorption capacity decreased with the increasing adsorbent loading and the maximum capacity of 1.31 mmol g^{-1} was achieved for 0.2 g of adsorbent and 0.2 L min^{-1} of flowrate. This behaviour could be associated with the presence of an unutilized mass of the oxide likely due to the cluttering of wet adsorbent particles in the adsorbent bed, which reduces the effective surface area for the reaction to occur[31]. However, no breakthrough experiment was conducted below 0.2 g. Since the material has a high density, loading adsorbent below 0.2 g led to a narrow bed length (since the tube diameter was 6 mm), which had a poor adsorbate-adsorbent interaction. The maximum adsorption capacity of 1.31 mmol g^{-1} achieved for the synthesized nanocomposite is similar to or higher than those reported for commercial ZnO (1.16 mmol g^{-1})[39], CeO_2-Mn_2O_3-Fe_2O_3 (0.83 mmol g^{-1})[28], Mn_2O_3-Fe_2O_3 (0.35 mmol g^{-1})[27], α-Fe_2O_3-Na_2SO_4 (1.06 mmol g^{-1})[29], and $ZnFe_2O_4$ (0.05 mmol g^{-1})[40] in similar experimental conditions.

The nanocomposite was also studied for SO_2 adsorption in dry and wet conditions (Fig. 5a). The adsorption capacity of 0.22 mmol g^{-1} in the dry condition nearly doubled to 0.41 mmol g^{-1} in the wet condition. Such

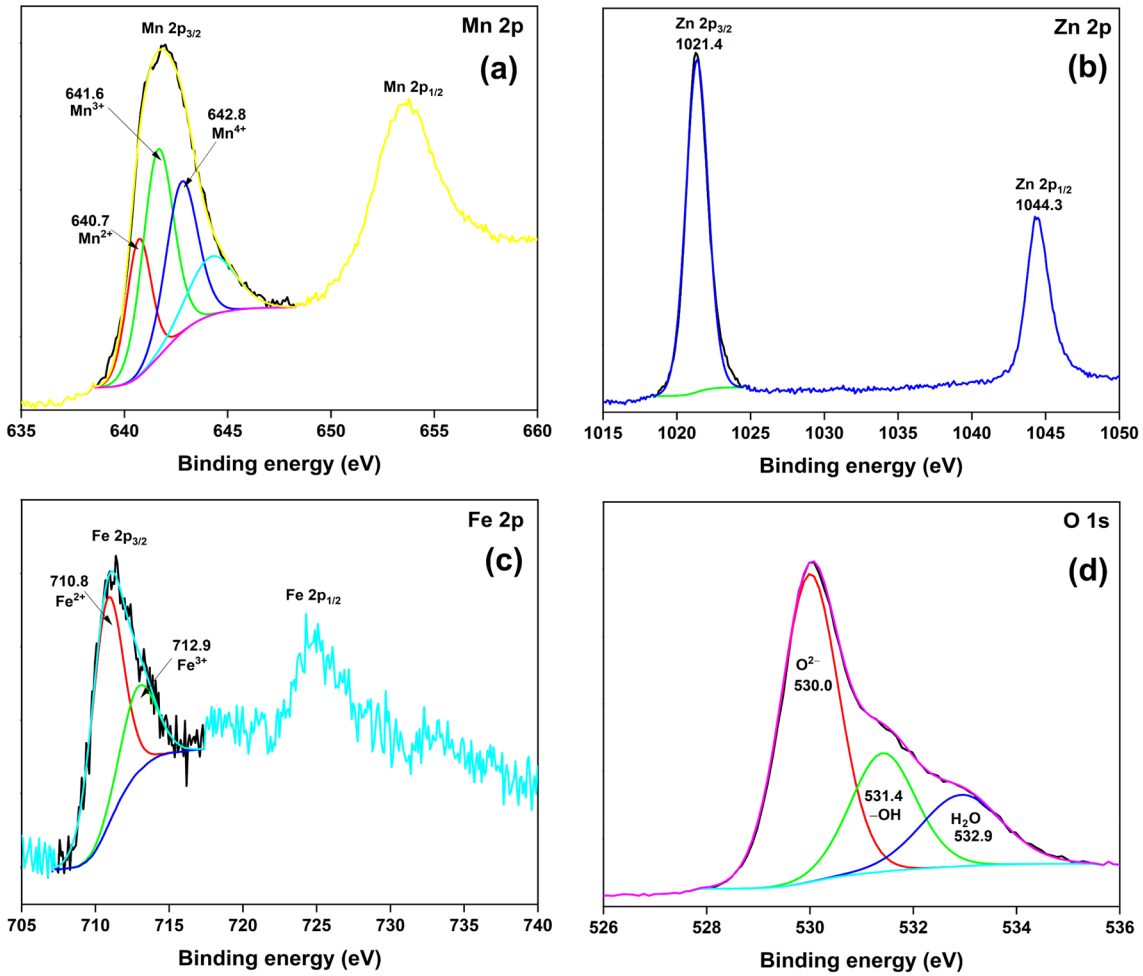

Figure 3. High-resolution XPS (**a**) Mn 2p; (**b**) Zn 2p; (**c**) Fe 2p; (**d**) O 1 s spectra of MFZO.

behaviour has been reported for oxidative SO_2 adsorption over MnO_2[16]. SO_2 adsorption in the presence of water molecules significantly accelerated the sulfate formation reaction, which favoured the overall adsorption process. The increasing gas flow rate negatively affected the adsorption process due to poor adsorbate-adsorbent interaction (Fig. 5b). The SO_2 adsorption capacity of the composite significantly improved with the decreasing adsorbent loading, where the maximum adsorption capacity of 0.49 mmol g^{-1} was confirmed with 0.2 g of adsorbent and 0.2 L min^{-1} of flowrate. Here also, the negative role of increasing bed loading was according to the effect witnessed for H_2S gas adsorption (Fig. 5c). Thus, in the optimized experimental conditions, the adsorbent could remove 0.49 mmol g^{-1} of SO_2 gas. This value is highly significant and comparable to the reported values for ZnO (0.28 mmol g^{-1})[41], MnO_2 (0.48–1.23 mmol g^{-1})[42], and NaM_xO_y (0.73 mmol g^{-1})[7] in similar experimental conditions. The nanocomposite possessed a higher H_2S adsorption capacity compared to the SO_2 gas. The superior H_2S adsorption was related to an easy dissociation of H_2S molecules due to the much lower energy barrier and higher adsorption energy compared to SO_2, which has been previously demonstrated for Zn–$MoSe_2$ structure through computational calculations[43].

The SEM and TEM micrographs post-H_2S and SO_2 adsorption showed no significant variation in the surface morphology (Figs. S1, S2) except for the transformation of a chunk of nanoparticles to cluttered nanorods. It could be due to the combined effect of moisture and gas acidity as the SEM micrographs of dry samples showed no such change in the surface morphology. The EDAX analysis of gas-exposed samples confirmed a new peak at ~ 2.3 keV for sulfur. The intensity of the S peak in the H_2S-adsorbed sample is much higher than that of the SO_2, which agreed with the experimental results (Fig. S3). The 2D elemental mapping of the H_2S and SO_2-adsorbed samples confirmed a high density of sulfur atoms over the oxide surface, which was uniformly distributed over the nanocomposite (Fig. 6).

The PXRD patterns of gas-exposed samples showed insignificant changes in the diffraction peaks, except for new peaks in the H_2S-adsorbed sample (marked as purple stars). These two peaks were assigned to the presence of $ZnSO_3$[44]. The absence of additional new peaks in these samples could be related to the formation of oxidized sulfur species on the surface (Fig. 7a). The N_2 adsorption–desorption isotherms are shown in Fig. 7b. For the H_2S-adsorbed sample, the surface area and pore volume decreased by 26 and 17%, respectively (Table 1). However, for the SO_2-exposed sample, a minimal drop in these values was observed. The drop in the surface area and porosity was linked to the deposition of oxidized sulfur species, which may have clogged the pores[29]. This

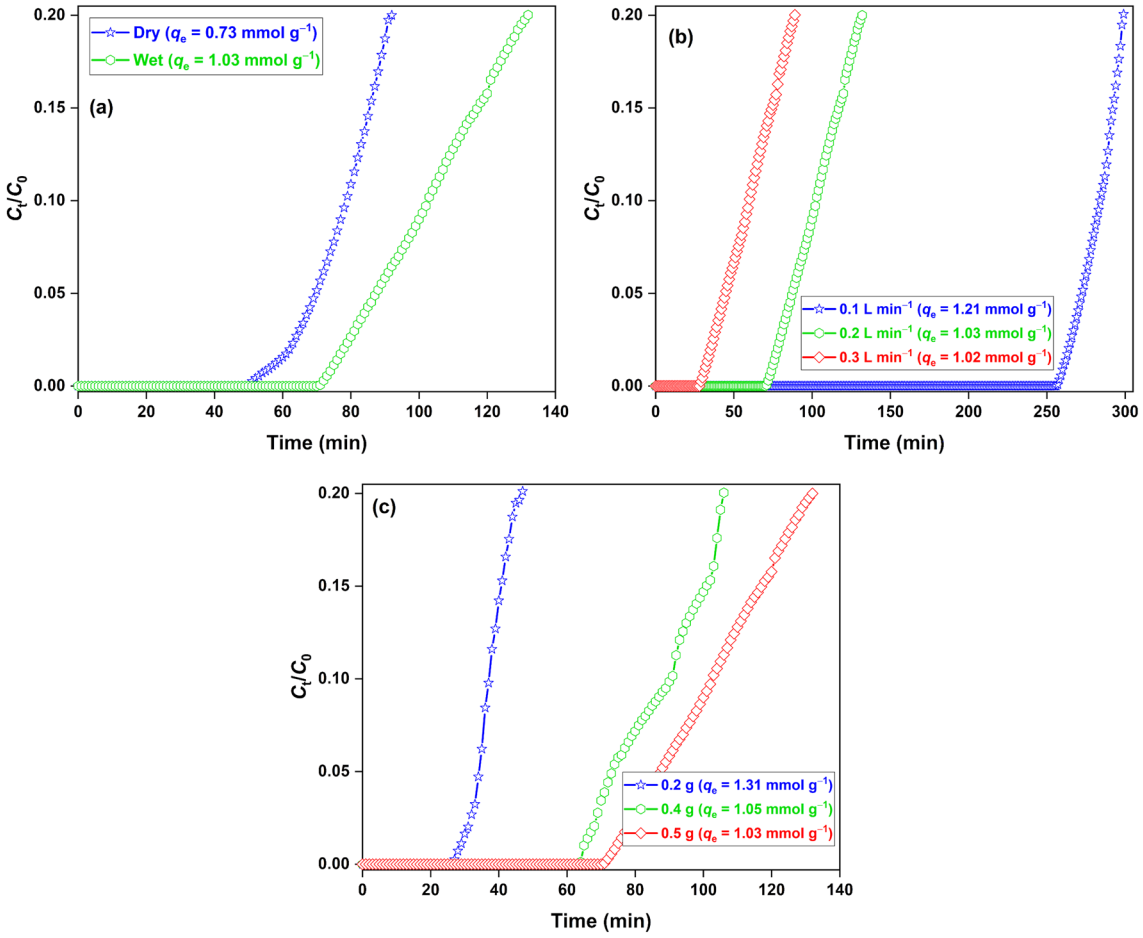

Figure 4. H_2S breakthrough curves for (**a**) dry/wet adsorbents; (**b**) wet adsorbent at different flowrate; (**c**) adsorbent loading. Conditions: [Adsorbent] = 0.5 g, flowrate = 0.2 L min^{-1} (changed otherwise).

clogging was expected more in the H_2S-adsorbed sample due to a higher gas volume adsorption and subsequent mineralization onto the surface.

More detailed information on the adsorption mechanism was deduced for the XPS analysis of MFZO nanocomposite after the gas adsorption process. In the HRXPS Mn 2p spectrum of the H_2S-adsorbed sample, all three contributions for Mn^{2+}, Mn^{3+}, and Mn^{4+} are present at a slightly lower binding energy with variation in the proportion of these oxidation species. The redshift in the binding energy could be associated with the partial sulfidation of the Mn oxides[31]. Moreover, the variation in the oxidation state proportions could be linked to the involvement of $Mn^{2+}/Mn^{3+}/Mn^{4+}$ redox cycles during the chemisorption process[17]. However, for SO_2-adsorbed samples, the only proportion of oxidation states varied with an insignificant shift in the position, which was related to the Mn redox behaviour responsible for the oxidation of SO_2 (Fig. 7c)[17,45]. The HRXPS Zn 2p spectrum of H_2S-adsorbed showed a minimal redshift in the peak position probably due to the formation of $ZnSO_3$ species. However, no such shift was witnessed for the SO_2-adsorbed sample, which further suggested the delocalized nature of the chemisorption process (Fig. 7d). In the HRXPS Fe 2p spectrum of H_2S-adsorbed MFZO, the peak position shifted slightly but with a minimal change in the proportion of Fe^{2+} and Fe^{3+} species. DFT calculations have predicted that H_2S dissociatively reacts better on the FeO (Fe^{2+} sites) than Fe_2O_3 (Fe^{3+} sites)[46]. Even in our previously reported work on the adsorption of H_2S over Mn_2O_3/Fe_2O_3, bulk Fe_2O_3 phase did not take part in the oxidation process[27]. The slight variation in the peak position could be linked to the involvement of Fe^{2+} sites in the H_2S adsorption process. For the SO_2-adsorbed sample, the Fe^{2+} and Fe^{3+} peak positions red-shifted by 0.1 and 0.4 eV, respectively, with a significant drop in the Fe^{2+} proportion (70.4–62.3%). It has been proven that the SO_2 molecules are much more reactive to the Fe^{2+} sites than the Fe^{3+} sites. Thus, a drop in the Fe^{2+} contribution suggested that the divalent Fe sites catered the oxidation of SO_2 molecules (Fig. 7e)[47]. In the HRXPS O 1 s spectrum of H_2S-adsorbed sample, the metal–oxygen bond contribution decreased, whereas the contribution at 531.6 eV for –OH/O–N increased due to the formation of metal-sulfide and sulfite (SO_3^-) species, respectively. For the SO_2-adsorbed sample, the 531.5 eV peak improved even further due to the consumption of lattice oxygen and the formation of sulfate species (Fig. 7f).

The HRXPS S 2p spectrum of H_2S-adsorbed MFZO was deconvoluted into three sets of doublets with their $2p_{3/2}$ peaks observed at 161.3, 163.6, and 167.9 eV for sulfide (36.1%), elemental sulfur (25.1%), and sulfite (38.8%)[48]. While the formation of metal-bound sulfide is initiated by the dissociated adsorption of H_2S (into H^+ and HS^-) in the presence of water molecules. The formation of elemental sulfur and sulfide is mediated by

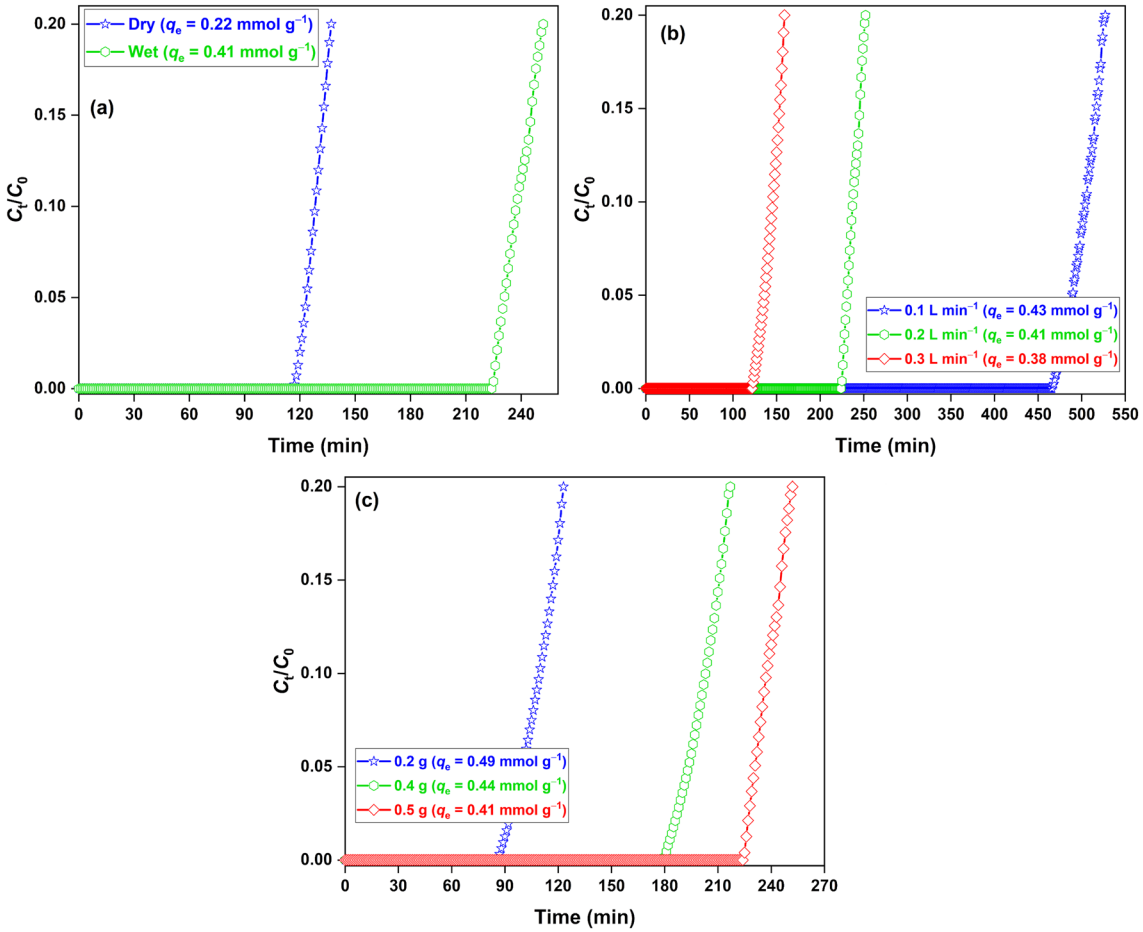

Figure 5. SO_2 breakthrough curves for (**a**) dry/wet adsorbent; (**b**) wet adsorbent at different flowrate; (**c**) wet adsorbent at different adsorbent loading. Conditions: [Adsorbent] = 0.5 g, flowrate = 0.2 L min^{-1} (changed otherwise).

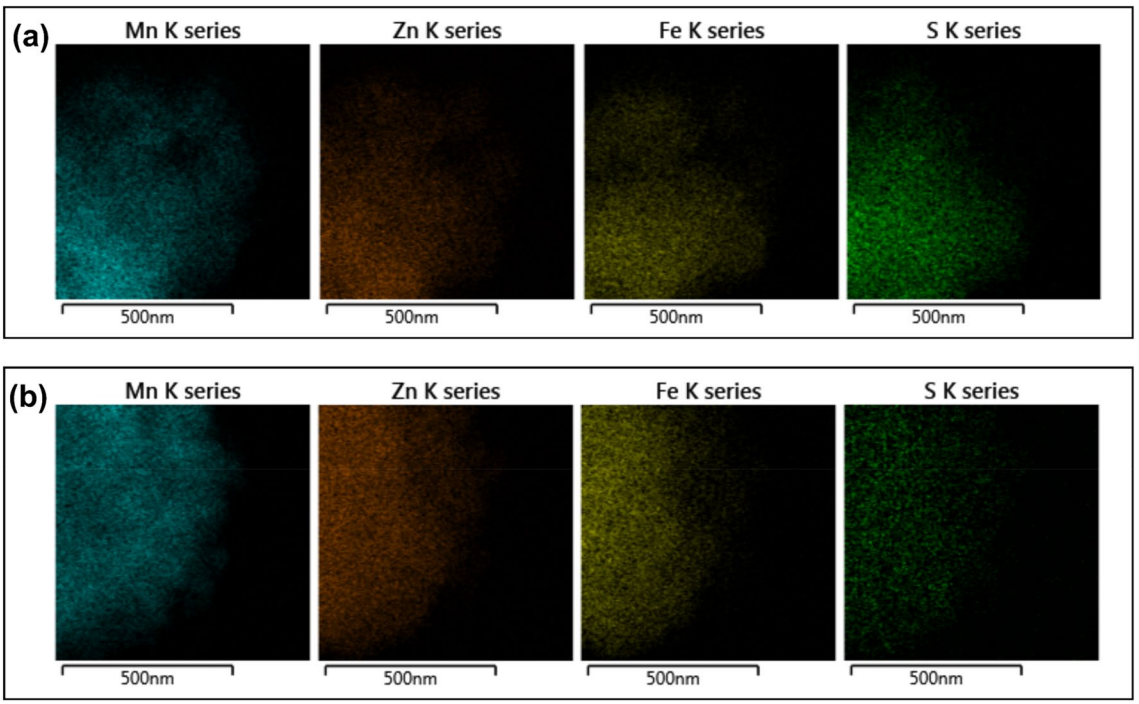

Figure 6. 2D elemental mapping of wet MFZO after (**a**) H_2S; (**b**) SO_2 adsorption.

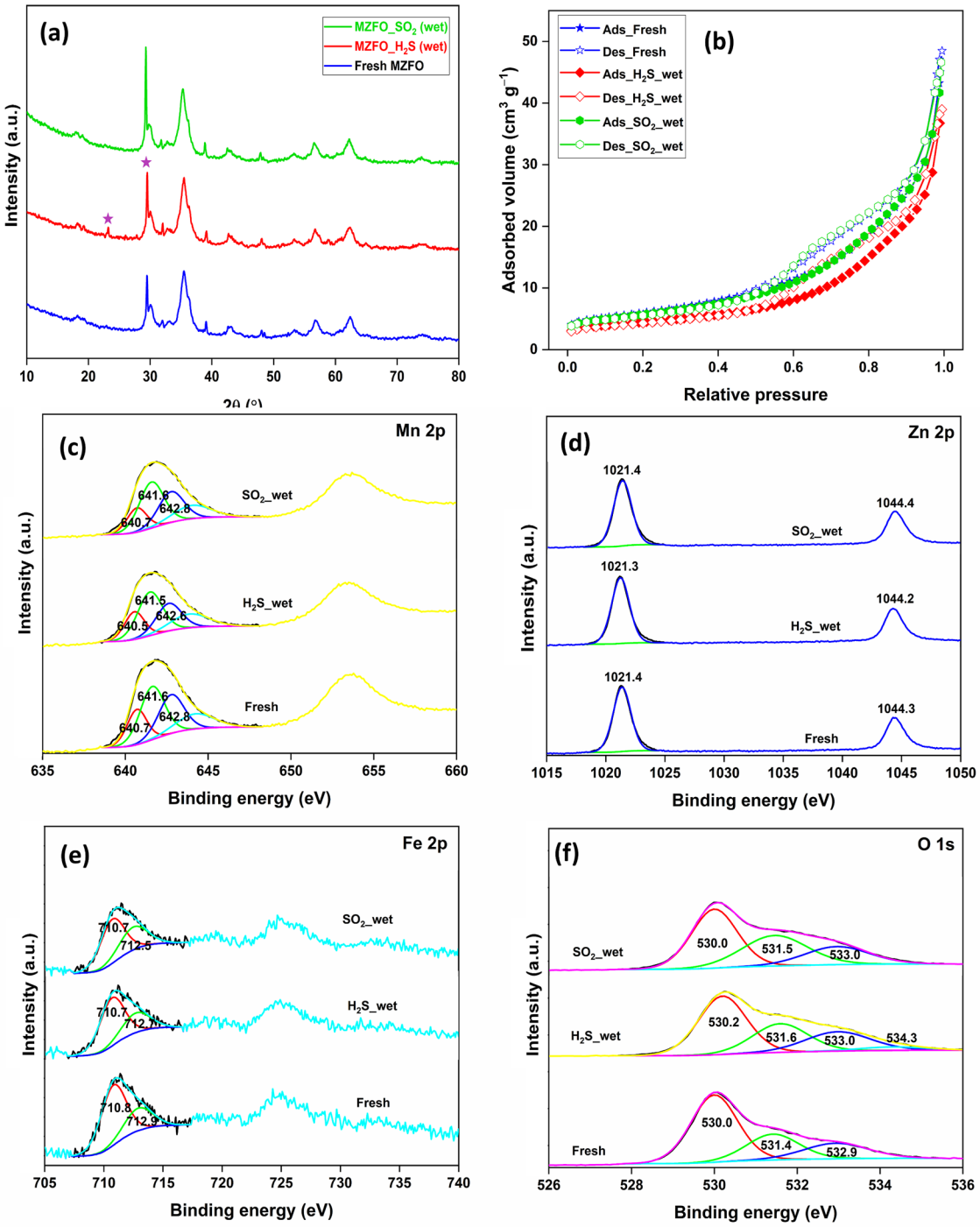

Figure 7. (**a**) PXRD patterns; (**b**) N_2 adsorption–desorption isotherms; High-resolution XPS (**c**) Mn 2p; (**d**) Zn 2p; (**e**) Fe 2p; (**f**) O 1 s spectra of wet MZFO after H_2S and SO_2 adsorption.

Sample	Surface area ($m^2\ g^{-1}$)	Pore volume ($cm^3\ g^{-1}$)	Average pore diameter (nm)
Fresh MFZO	21.03	0.070	13.4
MFZO_H_2S	15.56	0.058	14.8
MFZO_SO_2	20.16	0.068	13.4

Table 1. Surface area and pore characteristics of wet MFZO before and after gas adsorption.

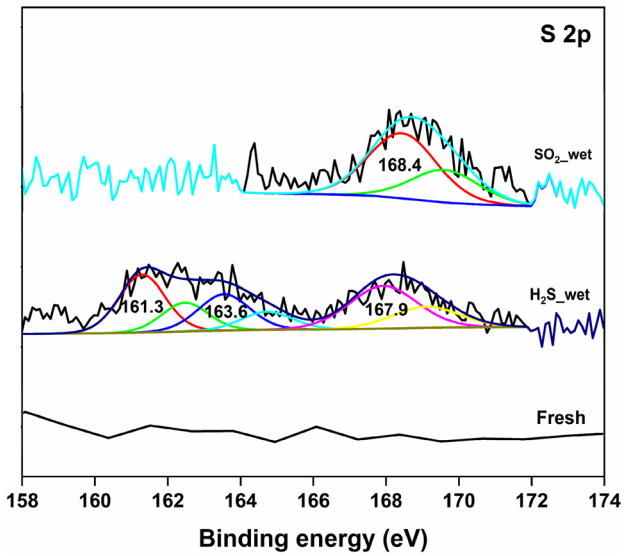

Figure 8. High-resolution XPS S 2p spectra of MFZO before and after H_2S and SO_2 adsorption.

the redox behaviour of transition metal ions, surface-adsorbed molecular oxygen, and water molecules[31]. Wang et al.have reported the dissociation of H_2S over In_2O_3 thin film in the presence of moisture, where the reactive dissociation of H_2S molecules with adsorbed water produced HS^- and H^+ species. The formed HS^- and H^+ ions reacted with the surface-chemisorbed oxygen species to yield sulfide and sulfite species[49]. The HRXPS S 2p spectrum of SO_2-adsorbed MFZO has a set of doublets with a $2p_{3/2}$ peak at 168.4 eV, which was assigned to the sulfate species (Fig. 8, Table S5)[48]. The adsorption of SO_2 over the oxide surface is generally driven by the reactive interaction of SO_2 molecules with the lattice oxygen or surface hydroxyl groups to form sulfite/bisulfite, which further oxidized to sulfate via redox behaviour of transition metal oxide and gaseous oxygen molecules[7,17]. Moreover, just like H_2S dissolution in the surface water, SO_2 could be readily adsorbed and hydrolysed by surface water molecules, which makes the oxidation of SO_2 molecules, energetically favourable[17].

Conclusion

In conclusion, we have fabricated an Mn-Zn-Fe metal oxide nanocomposite via a one-step coprecipitation reaction. The fabricated nanocomposite has MnO_2, ZnO, and ferrites with a surface area and pore volume of 21.03 $m^2\ g^{-1}$ and 0.07 $cm^3\ g^{-1}$, respectively. The nanocomposite was tested for room-temperature adsorptive removal of H_2S and SO_2 in dry and wet conditions. The oxide exhibited better gas adsorption capacity in wet conditions owing to the dissolution and dissociation of gaseous molecules in the surface water film. The adsorbent showed a better adsorption capacity at a lower flow rate and adsorbent loading. In the optimized conditions, a maximum of 1.31 and 0.49 mmol g^{-1} of H_2S and SO_2 was removed by the nanocomposite, respectively. The in-depth spectroscopic analysis confirmed the mineralization of H_2S gas into sulfide, sulfur, and sulfite, which was mediated by the Fe and Mn redox cycles in the presence of adsorbed water and molecular oxygen. Though Zn ions did not participate in the oxidation process, Zn^{2+} probably interacted with the sulfides and sulfites. The SO_2 mineralization was associated with the formation of sulfates, driven by the redox behaviour of Fe and Mn in an oxidative environment. Thus, we have presented a novel adsorbent material for the successful mineralization of toxic sulfurous gases, which could be suitable for deep desulfurization applications.

Data availability

Data is available from the corresponding author after reasonable request.

Received: 29 June 2022; Accepted: 5 September 2022
Published online: 13 September 2022

References

1. Shah, M. S., Tsapatsis, M. & Siepmann, J. I. Hydrogen sulfide capture: from absorption in polar liquids to oxide, zeolite, and metal-organic framework adsorbents and membranes. *Chem. Rev.* **117**, 9755–9803 (2017).
2. Habeeb, O. A., Kanthasamy, R., Ali, G. A. M., Sethupathi, S. & Yunus, R. B. M. Hydrogen sulfide emission sources, regulations, and removal techniques: a review. *Rev. Chem. Eng.* **34**, 837–854 (2018).
3. Mousa, H.A.-L. Short-term effects of subchronic low-level hydrogen sulfide exposure on oil field workers. *Environ. Health Prev. Med.* **20**, 12–17 (2015).
4. Ezoe, Y., Lin, C.-H., Noto, M., Watanabe, Y. & Yoshimura, K. Evolution of water chemistry in natural acidic environments in Yangmingshan Taiwan. *J. Environ. Monit.* **4**, 533 (2002).
5. Ruiz-López, M. F., Martins-Costa, M. T. C., Anglada, J. M. & Francisco, J. S. A new mechanism of acid rain generation from HOSO at the air–water interface. *J. Am. Chem. Soc.* **141**, 16564–16568 (2019).

6. Johns, D. O. & Linn, W. S. A review of controlled human SO_2 exposure studies contributing to the US EPA integrated science assessment for sulfur oxides. *Inhal. Toxicol.* **23**, 33–43 (2011).
7. Gupta, N. K., Bae, J., Baek, S. & Kim, K. S. Metal-organic framework-derived NaM_xO_y adsorbents for low-temperature SO_2 removal. *Chemosphere* **291**, 132836 (2021).
8. Perraud, V. *et al.* The future of airborne sulfur-containing particles in the absence of fossil fuel sulfur dioxide emissions. *Proc. Natl. Acad. Sci. USA* **112**, 13514–13519 (2015).
9. Shi, L., Yang, K., Zhao, Q., Wang, H. & Cui, Q. Characterization and mechanisms of H_2S and SO_2 adsorption by activated carbon. *Energy Fuels* **29**, 6678–6685 (2015).
10. Deng, J. *et al.* A review of NO_x and SO_x emission reduction technologies for marine diesel engines and the potential evaluation of liquefied natural gas fuelled vessels. *Sci. Total Environ.* **766**, 144319 (2021).
11. Waqif, M. *et al.* Comparative study of SO_2 adsorption on metal oxides. *Faraday Trans.* **88**, 2931 (1992).
12. Zhang, F. *et al.* Insight into the H_2S selective catalytic oxidation performance on well-mixed Ce-containing rare earth catalysts derived from MgAlCe layered double hydroxides. *J. Hazard. Mater.* **342**, 749–757 (2018).
13. Zhao, Y. *et al.* Critical role of water on the surface of ZnO in H_2S removal at room temperature. *Ind. Eng. Chem. Res.* **57**, 15366–15374 (2018).
14. Önsten, A. *et al.* Water adsorption on ZnO(0001): Transition from triangular surface structures to a disordered hydroxyl terminated phase. *J. Phys. Chem. C* **114**, 11157–11161 (2010).
15. Yang, C. *et al.* Bifunctional ZnO-MgO/activated carbon adsorbents boost H_2S room temperature adsorption and catalytic oxidation. *Appl. Catal. B* **266**, 118674 (2020).
16. Yang, W. *et al.* Heterogeneous reaction of SO_2 on manganese oxides: The effect of crystal structure and relative humidity. *Sci. Rep.* **7**, 4550 (2017).
17. Long, J. W., Wallace, J. M., Peterson, G. W. & Huynh, K. Manganese oxide nanoarchitectures as broad-spectrum sorbents for toxic gases. *ACS Appl. Mater. Interfaces* **8**, 1184–1193 (2016).
18. Gupta, N. K., Kim, S., Bae, J. & Kim, K. S. Chemisorption of hydrogen sulfide over copper-based metal–organic frameworks: methanol and UV-assisted regeneration. *RSC Adv.* **11**, 4890–4900 (2021).
19. Su, D., Ahn, H.-J. & Wang, G. β-MnO_2 nanorods with exposed tunnel structures as high-performance cathode materials for sodium-ion batteries. *NPG Asia Mater.* **5**, e70–e70 (2013).
20. Lu, H. *et al.* Novel ZnO microflowers on nanorod arrays: local dissolution-driven growth and enhanced light harvesting in dye-sensitized solar cells. *Nanoscale Res. Lett.* **9**, 183 (2014).
21. Thapa, B., Diaz-Diestra, D., Beltran-Huarac, J., Weiner, B. R. & Morell, G. Enhanced MRI T 2 relaxivity in contrast-probed anchor-free pegylated iron oxide nanoparticles. *Nanoscale Res. Lett.* **12**, 312 (2017).
22. Sannasi, V. & Subbian, K. Influence of Moringa oleifera gum on two polymorphs synthesis of MnO_2 and evaluation of the pseudo-capacitance activity. *J. Mater. Sci. Mater. Electron.* **31**, 17120–17132 (2020).
23. Tiwari, N. *et al.* Structural investigations of (Mn, Dy) co-doped ZnO nanocrystals using X-ray absorption studies. *RSC Adv.* **7**, 56662–56675 (2017).
24. Sharma, R., Bansal, S. & Singhal, S. Tailoring the photo-Fenton activity of spinel ferrites (MFe_2O_4) by incorporating different cations (M = Cu, Zn, Ni and Co) in the structure. *RSC Adv.* **5**, 6006–6018 (2015).
25. Su, Z. *et al.* A value-added multistage utilization process for the gradient-recovery tin, iron and preparing composite phase change materials (C-PCMs) from tailings. *Sci. Rep.* **9**, 14097 (2019).
26. Alam, M. W. *et al.* Novel copper-zinc-manganese ternary metal oxide nanocomposite as heterogeneous catalyst for glucose sensor and antibacterial activity. *Antioxidants* **11**, 1064 (2022).
27. Kim, S., Gupta, N. K., Bae, J. & Kim, K. S. Fabrication of coral-like Mn_2O_3/Fe_2O_3 nanocomposite for room temperature removal of hydrogen sulfide. *J. Environ. Chem. Eng.* **9**, 105216 (2021).
28. Gupta, N. K., Bae, J. & Kim, K. S. A novel one-step synthesis of Ce/Mn/Fe mixed metal oxide nanocomposites for oxidative removal of hydrogen sulfide at room temperature. *RSC Adv.* **11**, 26739–26749 (2021).
29. Gupta, N. K., Bae, J. & Kim, K. S. Iron-organic frameworks-derived iron oxide adsorbents for hydrogen sulfide removal at room temperature. *J. Environ. Chem. Eng.* **9**, 106195 (2021).
30. Phor, L. & Kumar, V. Self-cooling device based on thermomagnetic effect of MnxZn1−xFe2O4 (x = 0.3, 0.4, 0.5, 0.6, 0.7)/ferrofluid. *J. Mater. Sci. Mater. Electron.* **30**, 9322–9333 (2019).
31. Gupta, N. K., Bae, J. & Kim, K. S. Metal-organic framework-derived $NaMn_xO_y$ hexagonal microsheets for superior adsorptive-oxidative removal of hydrogen sulfide in ambient conditions. *Chem. Eng. J.* **427**, 130909 (2021).
32. Ren, H.-M., Cai, C., Leng, C.-B., Pang, S.-F. & Zhang, Y.-H. Nucleation kinetics in mixed $NaNO_3$ /glycerol droplets investigated with the FTIR–ATR technique. *J. Phys. Chem. B* **120**, 2913–2920 (2016).
33. Karthickraja, D. *et al.* Fabrication of core–shell $CoFe_2O_4$@HAp nanoparticles: a novel magnetic platform for biomedical applications. *New J. Chem.* **43**, 13584–13593 (2019).
34. Biesinger, M. C. *et al.* Resolving surface chemical states in XPS analysis of first row transition metals, oxides and hydroxides: Cr, Mn, Fe, Co and Ni. *Appl. Surf. Sci.* **257**, 2717–2730 (2011).
35. Gaddam, V. *et al.* Morphology controlled synthesis of Al doped ZnO nanosheets on Al alloy substrate by low-temperature solution growth method. *RSC Adv.* **5**, 13519–13524 (2015).
36. Majumder, S., Sardar, M., Satpati, B., Kumar, S. & Banerjee, S. Magnetization enhancement of Fe_3O_4 by attaching onto graphene oxide: An interfacial effect. *J. Phys. Chem. C* **122**, 21356–21365 (2018).
37. Idriss, H. On the wrong assignment of the XPS O1s signal at 531–532 eV attributed to oxygen vacancies in photo- and electro-catalysts for water splitting and other materials applications. *Surf. Sci.* **712**, 121894 (2021).
38. Long, N. Q. & Loc, T. X. Experimental and modeling study on room-temperature removal of hydrogen sulfide using a low-cost extruded Fe_2O_3-based adsorbent. *Adsorption* **22**, 397–408 (2016).
39. Wang, L.-J. *et al.* Design of a sorbent to enhance reactive adsorption of hydrogen sulfide. *ACS Appl. Mater. Interfaces* **6**, 21167–21177 (2014).
40. Yang, C., Florent, M., de Falco, G., Fan, H. & Bandosz, T. J. $ZnFe_2O_4$/activated carbon as a regenerable adsorbent for catalytic removal of H_2S from air at room temperature. *Chem. Eng. J.* **394**, 124906 (2020).
41. Gupta, N. K., Bae, J., Baek, S. & Kim, K. S. Sulfur dioxide gas adsorption over ZnO/Zn-based metal-organic framework nanocomposites. *Colloids Surf. A* **634**, 128034 (2022).
42. Ye, X. *et al.* Effect of manganese dioxide crystal structure on adsorption of SO_2 by DFT and experimental study. *Appl. Surf. Sci.* **521**, 146477 (2020).
43. Ayesh, A. I. DFT investigation of H_2S and SO_2 adsorption on Zn modified $MoSe_2$. *Superlattices Microstruct.* **162**, 107098 (2022).
44. Safarzadeh, M. S., Moradkhani, D., Ilkhchi, M. O. & Golshan, N. H. Determination of the optimum conditions for the leaching of Cd–Ni residues from electrolytic zinc plant using statistical design of experiments. *Sep. Purif. Technol.* **58**, 367–376 (2008).
45. Liu, X. C. *et al.* Development of low-temperature desulfurization performance of a MnO_2/AC composite for a combined SO_2 trap for diesel exhaust. *RSC Adv.* **6**, 96367–96375 (2016).
46. Lin, C., Qin, W. & Dong, C. H_2S adsorption and decomposition on the gradually reduced α-Fe_2O_3(001) surface: A DFT study. *Appl. Surf. Sci.* **387**, 720–731 (2016).
47. Toledano, D. S. & Henrich, V. E. Kinetics of SO_2 adsorption on photoexcited α-Fe_2O_3. *J. Phys. Chem. B* **105**, 3872–3877 (2001).

48. Fantauzzi, M., Elsener, B., Atzei, D., Rigoldi, A. & Rossi, A. Exploiting XPS for the identification of sulfides and polysulfides. *RSC Adv.* **5**, 75953–75963 (2015).
49. Wang, Y. *et al.* Room temperature H_2S gas sensing properties of In_2O_3 micro/nanostructured porous thin film and hydrolyzation-induced enhanced sensing mechanism. *Sens. Actuators B* **228**, 74–84 (2016).

Acknowledgements
This research was funded by [Project #20220145-001] provided by the "Korea Institute of Civil Engineering and Building Technology" (KICT), Korea.

Author contributions
N.K.G. was responsible for conceptualization, formal analysis, software, writing original drafts, and review and editing. N.K.G., E.J.K., and S.B. oversaw data curation, methodology, visualization, and validation. J.B. and K.S.K. were responsible for funding acquisition, investigation, project administration, resources, and supervision. All authors have read and agreed to the submitted version of the manuscript.

Competing interests
The authors declare no competing interests.

Additional information
Supplementary Information The online version contains supplementary material available at https://doi.org/10.1038/s41598-022-19800-6.

Correspondence and requests for materials should be addressed to J.B. or K.S.K.

Reprints and permissions information is available at www.nature.com/reprints.

Publisher's note Springer Nature remains neutral with regard to jurisdictional claims in published maps and institutional affiliations.